

Simultaneous, accurate measurement of the 3D position and orientation of single molecules

Mikael P. Backlund^{a,1}, Matthew D. Lew^{a,b,1}, Adam S. Backer^{a,c}, Steffen J. Sahl^a, Ginni Grover^d, Anurag Agrawal^d, Rafael Piestun^d, and W. E. Moerner^{a,2}

Departments of ^aChemistry and ^bElectrical Engineering and ^cInstitute for Computational and Mathematical Engineering, Stanford University, Stanford, CA 94305; and ^dDepartment of Electrical, Computer, and Energy Engineering, University of Colorado, Boulder, CO 80309

Contributed by W. E. Moerner, September 25, 2012 (sent for review July 24, 2012)

Recently, single molecule-based superresolution fluorescence microscopy has surpassed the diffraction limit to improve resolution to the order of 20 nm or better. These methods typically use image fitting that assumes an isotropic emission pattern from the single emitters as well as control of the emitter concentration. However, anisotropic single-molecule emission patterns arise from the transition dipole when it is rotationally immobile, depending highly on the molecule's 3D orientation and *z* position. Failure to account for this fact can lead to significant lateral (*x*, *y*) mislocalizations (up to ~50–200 nm). This systematic error can cause distortions in the reconstructed images, which can translate into degraded resolution. Using parameters uniquely inherent in the double-lobed nature of the Double-Helix Point Spread Function, we account for such mislocalizations and simultaneously measure 3D molecular orientation and 3D position. Mislocalizations during an axial scan of a single molecule manifest themselves as an apparent lateral shift in its position, which causes the standard deviation (SD) of its lateral position to appear larger than the SD expected from photon shot noise. By correcting each localization based on an estimated orientation, we are able to improve SDs in lateral localization from ~2× worse than photon-limited precision (48 vs. 25 nm) to within 5 nm of photon-limited precision. Furthermore, by averaging many estimations of orientation over different depths, we are able to improve from a lateral SD of 116 (~4× worse than the photon-limited precision; 28 nm) to 34 nm (within 6 nm of the photon limit).

The recent emergence of superresolution far-field optical microscopy techniques has provided a means for attaining resolution beyond the diffraction limit (~250 nm) in noninvasive fluorescence imaging of biological structures (1, 2). Some of these techniques [including (f)PALM (3, 4), STORM (5), and PAINT (6)] rely on precise localization of sparse subsets of single-molecule (SM) emitters to surpass the diffraction limit by up to an order of magnitude (precisions of tens of nanometers). Collectively, these SM-based superresolution techniques can be grouped under the name SM Active Control Microscopy (SMACM), because they all rely on using various experimental strategies (photoactivation, switching, blinking additives, etc.) to maintain a very low concentration of emitters in each imaging frame, enabling the localization of SMs without overlap. Typically, the SM fitting uses estimators that assume isotropic emission, i.e., that the center of the photon distribution of an SM image corresponds directly to the true position of the molecule. Examples of these estimators include centroid finding, least-squares fitting to a 2D Gaussian function, and maximum likelihood methods that assume isotropic emitters.

However, immobile fluorescing SMs produce an inherently anisotropic emission pattern that depends on the orientation of the SM emission dipole moment relative to the optical axis (7, 8). The work by Enderlein et al. (9) has shown that fitting such an SM image to a 2D Gaussian can result in position errors of tens of nanometers for molecules located in the microscope's focal plane. Even more strikingly, the work by Engelhardt et al. (10) noted that, with modest defocusing (*z* = ±300 nm), the position error associated with fitting to a centroid can exceed 100 nm for certain SM dipole orientations. If labels are sufficiently rotationally mobile such that they explore much of the orientation

space within a single acquisition, this effect is averaged away, and accuracy can be recovered. However, in some cases, labels of biological structures can exhibit well-defined orientations (11). Furthermore, fluorophores can be purposely anchored to convey orientation information about biological macromolecules, such as work in various SM studies on motor protein translocation (12–14). Although this position error has important implications for 2D SMACM techniques, the implications for 3D SMACM techniques are even more significant. Namely, techniques such as astigmatism (15), multiplane (16), iPALM (17), and Double-Helix Point Spread Function (DH-PSF) (18) imaging depend explicitly on precise 3D localization of SMs over an extended depth of field of up to ~2 μm. Failure to account for this dipole orientation effect can clearly lead to large position inaccuracies that severely limit the superresolving capabilities of these techniques. Of these 3D methods, the DH-PSF is uniquely suited to address orientation effects, because its double-lobed shape results from the superposition of various waves in the microscope's pupil plane that converge and interfere in the image plane; the intensities of these waves are strongly affected by the dipole radiation pattern of SMs.

There are many established methods for determining dipole orientation of single fluorophores. Approaches have been developed that rely on excitation and/or emission with multiple polarizations (19, 20), introduction of defocus and pattern matching (21), direct imaging of pupil functions (22), and use of annular illumination to create characteristic field distributions (23) to name a few. The alternating measurement of 2D position and orientation has also been addressed (24). Two groups considered simultaneous 2D localization and orientation fitting for molecules located in the focal plane (25) or molecules at a known defocus (26). However, neither explicitly addresses the correction of systematic errors on the order of 50–100 nm, and these methods require fine sampling and accurate fitting of detailed patterns in SM images. This paper shows simultaneous measurement of precise and accurate 3D localization and molecular orientation. We account for and correct large localization errors using an adaptation of the established DH-PSF method.

The basics of the DH-PSF microscope have been described in detail elsewhere (18). Briefly, the DH-PSF causes a single fluorescent emitter to appear on the detector as two closely spaced lobes. Here, we use an estimator based on fitting the two lobes with two Gaussian functions. Precise *x* and *y* localization can be extracted from the midpoint (*x*, *y*) position between the two lobes, whereas precise *z* localization is determined by the angle of the axis connecting the two lobes. As an emitter is moved in *z*, the DH-PSF revolves, effectively tracing out a double helix along

Author contributions: M.P.B., M.D.L., R.P., and W.E.M. designed research; M.P.B., M.D.L., A.S.B., and G.G. performed research; S.J.S. and A.A. contributed new reagents/analytic tools; M.P.B., M.D.L., and A.S.B. analyzed data; and M.P.B., M.D.L., A.S.B., A.A., R.P., and W.E.M. wrote the paper.

The authors declare no conflict of interest.

¹M.P.B. and M.D.L. contributed equally to this work.

²To whom correspondence should be addressed. E-mail: wmoerner@stanford.edu.

This article contains supporting information online at www.pnas.org/lookup/suppl/doi:10.1073/pnas.1216687109/-DCSupplemental.

the optical axis and thus, encoding the z position in the angle of revolution calibrated separately by z translation of a fluorescent bead. In the experimental implementation (Fig. 1A), the DH-PSF response is generated by convolution with the standard SM image using an appropriate phase mask at the Fourier plane of a $4f$ imaging system built directly after the intermediate image plane of a standard microscope. Typically, the phase mask is loaded onto a phase-only reflective liquid crystal spatial light modulator (SLM) (27–29). This type of SLM can only modulate vertically polarized light, and therefore, the emission must be polarized before being detected. Previously, a dual-polarization DH-PSF microscope was described, in which two orthogonal polarizations were split by a polarizing beam splitter, the horizontally polarized channel was rotated with a $\lambda/2$ wave plate, and each polarization channel was then reflected separately off the SLM at necessarily disparate angles of incidence (30). This scheme is not ideal for our application, because the different angles of incidence on the SLM cause each channel to incur dissimilar aberrations. For the measurement in this paper, it was necessary to detect the two polarization channels with maximal channel symmetry provided by the setup shown in Fig. 1B. The two polarization channels are forced to have the same angle of incidence on the SLM by making use of a square pyramidal mirror to deflect the beams out of the plane into the w direction (marked in Fig. 1B–D) and onto the SLM mounted from above with its face to the mirror (Fig. 1C and D). Polarized images are measured with two orthogonal orientations of the phase mask (Fig. 1B Inset) for reasons described below.

It is well-known that splitting emission into orthogonal polarization channels alone yields some information about an emitter's azimuthal (ϕ) (Fig. 1A Insets) orientation based on the computed linear dichroism,

$$LD = \frac{N_T - N_R}{N_T + N_R} \approx \cos(2\phi), \quad [1]$$

in which N_T and N_R are the numbers of photons detected above background in the transmitted and reflected polarization channels, respectively, and the last equality is exact only if the partially depolarizing effect of high numerical aperture (N.A.) optics is ignored. Here, transmitted and reflected are defined

relative to the polarizing beam splitter (Fig. 1B). Clearly, LD is related to the projection of an SM dipole onto the detection polarizations, which in turn, is related to ϕ , but there exist degeneracies if LD is the only recorded measurement (12). To break degeneracies and measure polar orientation (θ) (Fig. 1A Insets), another parameter must be measured. Interestingly, the DH-PSF uniquely offers such a parameter. Namely, the relative intensity of the two lobes of the DH-PSF is actually a function of (z, θ, ϕ) of an SM emitter. Whereas an isotropic point source yields lobes of equal intensity for all z when convolved with the DH-PSF, our simulations (*vide infra*) show that images of SM dipoles can exhibit large lobe asymmetries (LA) for certain orientations at various values of defocus (Fig. 2A). Qualitatively, this asymmetry is introduced because the asymmetric pupil functions of SM dipoles (22) are multiplied by the DH-PSF phase mask, causing various spatial frequencies of the ordinary DH-PSF to be attenuated as a function of orientation and defocus. We quantify the lobe asymmetry as

$$LA = \frac{A_{L1} - A_{L2}}{A_{L1} + A_{L2}}, \quad [2]$$

in which A_{L1} and A_{L2} are the amplitudes (as determined by a nonlinear least squares fit to a double Gaussian function) of lobes 1 and 2 of the DH-PSF, respectively. By measuring (z, LD, LA) from DH-PSF images of an emitter, we are, thus, able to determine the molecule's orientation as described below.

Simulations

We simulated the DH-PSF response to dipole orientation based on full vectorial diffraction calculations (21), in which dipole emitters are embedded in a polymer at a fixed distance below the air-polymer interface (*SI Text* and Fig. S1). The polarized electric field distributions from this calculation were propagated to the intermediate image plane and convolved with the DH-PSF as in the experimental setup, and the final images (Fig. 2A) were fit with a double Gaussian estimator (*SI Text* and Fig. S2). This procedure was repeated for various (z, θ, ϕ) to sample the functions $LD(z, \theta, \phi)$ and $LA(z, \theta, \phi)$ at resolution ($\delta z = 50$ nm, $\delta \theta \sim 6.5^\circ$, $\delta \phi \sim 6.5^\circ$). Fig. 2B–D shows a z cross-section of this

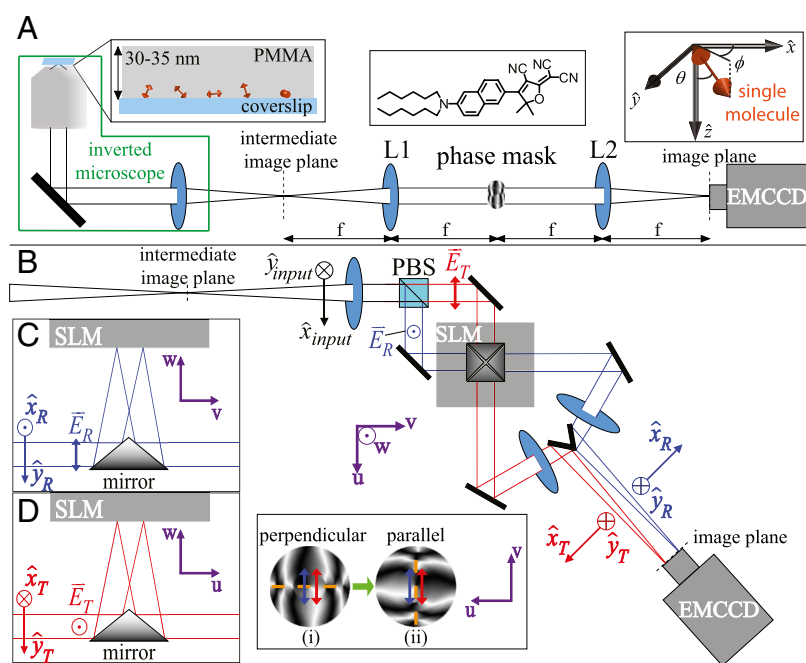


Fig. 1. DH-PSF imaging system. (A) Inverted microscope and $4f$ optical system schematic, where L1 and L2 are focal length-matched achromatic lenses. Our sample for the experiments described consisted of DCDHF-N-6 molecules (Center Inset) embedded in a thin layer of PMMA (Left Inset). Orientation angles (θ, ϕ) are defined in Right Inset and have ranges $(0^\circ, 90^\circ)$ and $(-180^\circ, 180^\circ)$, respectively. (B) The high efficiency dual-polarization detection DH-PSF setup used for these experiments (inverted microscope omitted for simplicity). The collected fluorescence is split by a polarizing beam splitter (PBS) into reflected (R; blue) and transmitted (T; red) channels. Input Cartesian unit vectors $(\hat{x}_{input}, \hat{y}_{input})$ define molecular orientation (θ, ϕ) and are propagated differently through the various reflections in the two polarization channels $[(\hat{x}_R, \hat{y}_R)$ and $(\hat{x}_T, \hat{y}_T)]$. The two electric field polarization axes \hat{E}_R and \hat{E}_T are projected identically onto the phase mask (Inset). Inset shows how each polarization axis (blue and red arrows) is oriented relative to the mask's axis of phase discontinuities (dashed orange) when the mask is upright (i; polarization perpendicular to discontinuities) and rotated (ii; polarization parallel to discontinuities). (C and D) Two side-on views of the SLM portion of the setup showing the square pyramidal mirror.

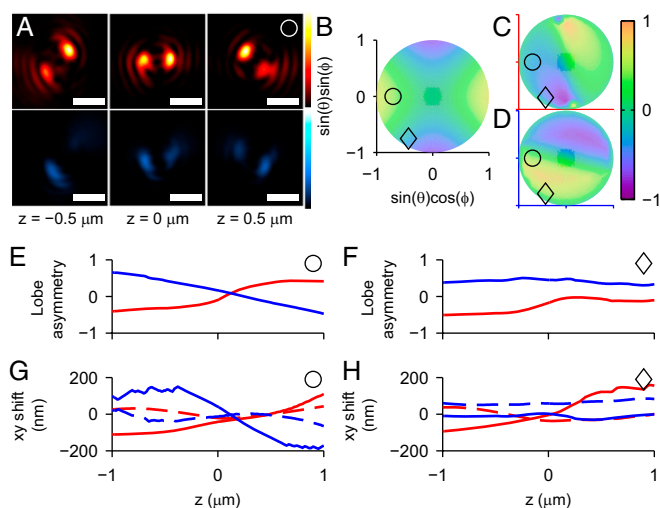


Fig. 2. Simulated behavior of the DH-PSF response to dipole orientation. (A) Example DH-PSF images of a molecule with orientation ($\theta = 45^\circ$, $\phi = 180^\circ$) at several z positions. *Upper* (red) shows images that appear in the parallel polarization channel, whereas *Lower* (blue) shows images from the perpendicular polarization channel (definitions in the text). (Scale bar: 1 μm .) (B) A z cross-section ($z = -500$ nm) of LD as a function of (θ, ϕ) , where (θ, ϕ) are projected into rectangular coordinates according to the relations marked on the axes. The center of the plot corresponds to a dipole aligned with the optical axis ($\theta = 0^\circ$), whereas the perimeter of the plot corresponds to molecules with $\theta = 90^\circ$; ϕ is the azimuthal angle from the positive x axis that increases in a counterclockwise direction. The points marked with \circ and \diamond correspond to the orientations ($\theta = 45^\circ$, $\phi = 180^\circ$) and ($\theta = 60^\circ$, $\phi = -120^\circ$), respectively. (C and D) Corresponding plots showing the functional behavior of LA vs. orientation for constant $z = -500$ nm in the parallel (C; red axes) and perpendicular (D; blue axes) channels, respectively. (E) LA vs. z in the parallel (red) and perpendicular (blue) channels for a fixed example dipole orientation (\circ). (F) The same plot for a different orientation (\diamond). (G) Δx (solid line) and Δy (dashed line) vs. z in the two channels for the \circ orientation. (H) The same plot for the \diamond orientation.

functional behavior, linearly interpolating between samples, whereas Fig. 2 E and F gives two examples of how LA varies with z for fixed (θ, ϕ) . Notably, LA has a distinct functional form in each of the parallel and perpendicular polarization channels (where parallel and perpendicular refer to the relative orientation between the axis of polarization and the axis of phase discontinuities in the DH-PSF phase mask) (Fig. 1B *Inset*) because of the fact that the asymmetry of the phase mask itself breaks the degeneracy of the two channels. From the estimator fit, we also mapped the apparent lateral shifts (Δx , Δy) associated with the DH-PSF as a function of (z, θ, ϕ) . Fig. 2 G and H shows that this shift can, indeed, be on the order of ~ 200 nm, similar to the behavior of the standard PSF (10). In general, more highly inclined molecules (θ closer to 0°) tend to exhibit both larger LA and larger (Δx , Δy).

These simulations provided a library that was used to fit orientation and correct the associated position error of a real measurement using the following algorithm. First, polarized DH-PSF images were fit with a double Gaussian estimator, yielding the observables ($x_{\text{apparent}}, y_{\text{apparent}}, z, LA, LD$). The apparent lateral position ($x_{\text{apparent}}, y_{\text{apparent}}$) is the true lateral position of the molecule ($x_{\text{true}}, y_{\text{true}}$) plus the apparent lateral shift (Δx , Δy) caused by the dipole emission effect. Second, (z, LA, LD) were fed to the simulated look-up table to give an estimate of the orientation (θ, ϕ). Third, (z, θ, ϕ) were referenced by the simulation to give a predicted (Δx , Δy) that was then subtracted from ($x_{\text{apparent}}, y_{\text{apparent}}$) to recover the true lateral position of the molecule: ($x_{\text{true}}, y_{\text{true}}$). In principle, SM dipole emission also causes errors in the double Gaussian-based estimate of z ; however, our simulations show that this error is small compared with

our precision in z . Here, we neglect this effect, but in principle, it can be corrected by extending the scheme above.

Experimental Validation

To show our ability to fit orientation and correct apparent shifts, we recorded SM images using the setup in Fig. 1B. Samples consisted of dicyanomethylenedihydrofuran-N-6 (DCDHF-N-6) (31) molecules spun in a layer of poly(methyl methacrylate) (PMMA) (Fig. 1A *Insets*) that provided a rigid enough environment such that angular flexibility of the dipole orientation was minimized. For a given field of view, the objective was scanned over z in 50-nm steps over a 2- μm total depth range (DR) centered about the focal plane. Images were recorded at every z step, and therefore, for each SM, many different sets of observables ($x_{\text{apparent}}, y_{\text{apparent}}, z, LA, LD$) were recorded. From each single measurement of this set, we estimated orientation and 3D position according to the prescription detailed above, and ultimately, we subtracted lateral shifts (Δx , Δy) from the apparent positions. Because we do not expect the orientation or lateral position of an SM to change on our imaging timescale for PMMA at room temperature, each independent measurement should produce the same ($x_{\text{true}}, y_{\text{true}}, \theta, \phi$) within some precision. In other words, our method is validated if the determined ($x_{\text{true}}, y_{\text{true}}, \theta, \phi$) of an SM are each constant functions of z .

Simulations show that the DH-PSF dipole response is dependent on E -field polarization, as a consequence of the asymmetry of the phase mask. Because of the geometry of our setup, however, the polarization axis of each polarization channel is identical in the SLM plane (propagation of \vec{E}_R and \vec{E}_T in Fig. 1 B–D). This property of our optical system has the effect of rendering both experimental polarization channels with either parallel-type behavior or perpendicular-type behavior, depending on the orientation of the mask (Fig. 1B *Inset*). Thus, to capture the full behavior of the DH-PSF response to dipole emission patterns, we measured each SM with the mask oriented upright (perpendicular) and rotated by 90° (parallel). It is important to note that the two simultaneously recorded images (in the T and R channels) are not identical and do not purvey degenerate information, despite both exhibiting parallel-/perpendicular-type behavior, because the molecular coordinates are projected differently onto the mask in the T and R channels. Hence, we used nondegenerate information provided from four different images (two acquisitions of two polarization channels) of each SM to produce a single estimate of ($x_{\text{true}}, y_{\text{true}}, \theta, \phi$). We collected $\sim 3,000$ – $8,500$ (Table S1) total photons per set of four images, a number on the same order as typical SMACM measurements, but the high stability of the SMs allowed this collection to be done for many z positions.

As an independent verification of these orientation estimates, we also measured orientation directly through defocused images of SMs using the standard PSF (21). The defocused images were acquired by toggling off the DH-PSF phase mask (thereby invoking a clear aperture) and defocusing the microscope objective by 1.00 ± 0.15 μm away from the sample. By comparing these images with simulations using template matching (SI Text and Fig. S3), we extracted a separate estimate of (θ, ϕ). Interestingly, we found it necessary to correct primary astigmatism and coma using the SLM and include spherical aberration in our simulations to match experimental images to simulated ones (SI Text). DH-PSF orientation estimation, however, did not require accounting for these aberrations explicitly to produce the results described below [although some amount is included implicitly in the calibrated DH-PSF response of (x, y) vs. z] (SI Text). Because the DH-PSF mask itself works by imparting a sizeable distortion on the wave front, the associated images seem to be more robust to minor disturbances of the wave front caused by aberrations (32).

Results and Discussion

Using our DH-PSF-based method, we estimated the orientations of six SMs (two example molecules are shown in Fig. 3, and more examples are shown in Fig. S4). To distinguish the four images,

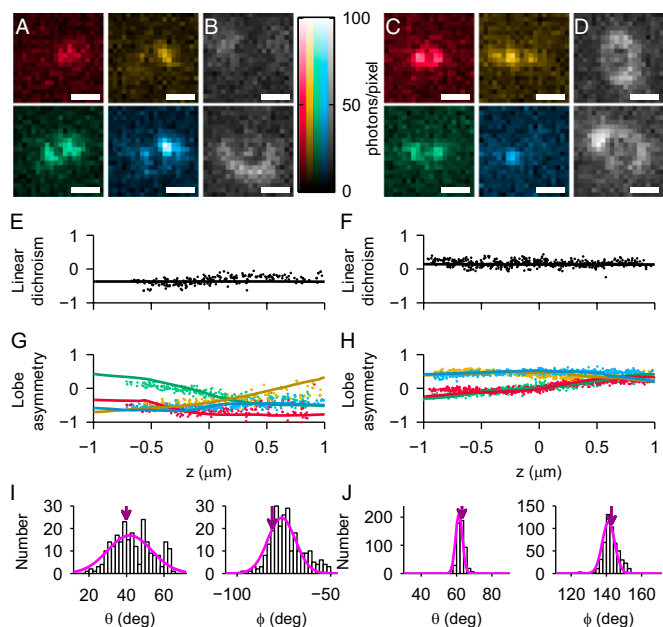


Fig. 3. Orientation fitting results for example molecule 1 (A, B, E, G, and I) and example molecule 2 (C, D, F, H, and J). (Scale bars: 1 μm .) (A) Four example DH-PSF images (which constitute one measurement of orientation) of molecule 1 at $z \sim -250$ nm as it appears in each of four mask orientation/polarization channel combinations: red, gold, green, and blue (definitions in the text). Note that only one lobe is easily visible in the red and gold channels. (B) The transmitted (Upper) and reflected (Lower) polarization defocused standard PSF images used for independent orientation measurement. (C) The equivalent of A for example molecule 2 at $z \sim 0$ nm. (D) The equivalent of B for example molecule 2. (E and F) Each measurement of LD (scatter points) and the predicted LD based on the mean fit orientation (solid line) for each molecule. (G and H) Each measurement of LA in each channel (color code is the same as in A) and the overlaid predicted LA for the mean fit orientation. (I and J) Histograms of θ and ϕ extracted from DH-PSF based measurements. Magenta line is Gaussian fit. Purple arrow denotes orientation extracted from defocused imaging.

we assigned colors to each mask orientation/polarization combination: mask parallel/transmitted polarization is the red channel, mask perpendicular/transmitted polarization is the gold channel, mask parallel/reflected polarization is the green channel, and mask perpendicular/reflected polarization is the blue channel. Fig. 3 A and C shows representative images of the DH-PSF for each example molecule in the four channels at a single z position, whereas Fig. 3 B and D shows the corresponding clear-aperture defocused images. For both example molecules, we show each measurement of LD (Fig. 3 E and F) and LA (Fig. 3 G and H) as a scatter point plotted vs. z . For each quartet of LA measurements and associated LD measurements, there is a corresponding estimation of (θ, ϕ) . The mean orientation of the Gaussian fit of these distributions of (θ, ϕ) yields the solid overlays in Fig. 3 E–H. The full distributions of DH-PSF-extracted (θ, ϕ) are shown in Fig. 3 I and J. The sequential build up of these histograms as the objective was scanned for molecule 1 is shown in [Movie S1](#). Also displayed for each molecule in Fig. 3 I and J is the orientation estimated from our independent defocused measurement (Fig. 3 I and J, purple arrows). We show excellent agreement between the defocus-determined orientation and the DH-PSF-based measurements: $(\theta_{\text{DH-PSF}} = 42^\circ \pm 12^\circ, \phi_{\text{DH-PSF}} = -76^\circ \pm 7^\circ)$ and $(\theta_{\text{defocus}} = 40^\circ \pm 2^\circ, \phi_{\text{defocus}} = -81^\circ \pm 4^\circ)$ for molecule 1; $(\theta_{\text{DH-PSF}} = 61^\circ \pm 2^\circ, \phi_{\text{DH-PSF}} = 141^\circ \pm 4^\circ)$ and $(\theta_{\text{defocus}} = 63^\circ \pm 3^\circ, \phi_{\text{defocus}} = 143^\circ \pm 5^\circ)$ for molecule 2. The SDs of each distribution (2° – 12°) are comparable with the SDs of other methods (12).

Apparent shift corrections for these example molecules are shown in various ways in Fig. 4. First, $(\Delta x, \Delta y)$ are plotted as functions of z and overlaid again with those predictions for the mean orientation fit (Fig. 4 A–D). By binning the (x, y) positions of both SMs recorded across our entire 2- μm DR, we produced the 2D histograms shown in Fig. 4 E and F. For an isotropic emitter, for which $(x_{\text{apparent}}, y_{\text{apparent}})$ does not depend on z , the 2D distribution should be circularly symmetric, with width approximately proportional to $1/\sqrt{N}$, where N is the number of photons collected in that channel. Because of the dipole effect, the uncorrected distributions have irregular, elongated shapes in some cases (e.g., the green channel of molecule 1 and the green and red channels of molecule 2). By subtracting the apparent shifts $(\Delta x, \Delta y)$ predicted from each individual fit of orientation, we recovered the corrected distributions shown in Fig. 4 G and H. Importantly, cases that were elongated and irregularly shaped when uncorrected became more concentrated and symmetric when corrected. Uncorrected cases that were relatively concentrated and symmetric to begin with did not undergo much change upon correction (e.g., the gold channel of molecule 2). The gold channel of molecule 1 shows a case where a large (>200 nm) shift is followed closely by simulation and removed on correction, but

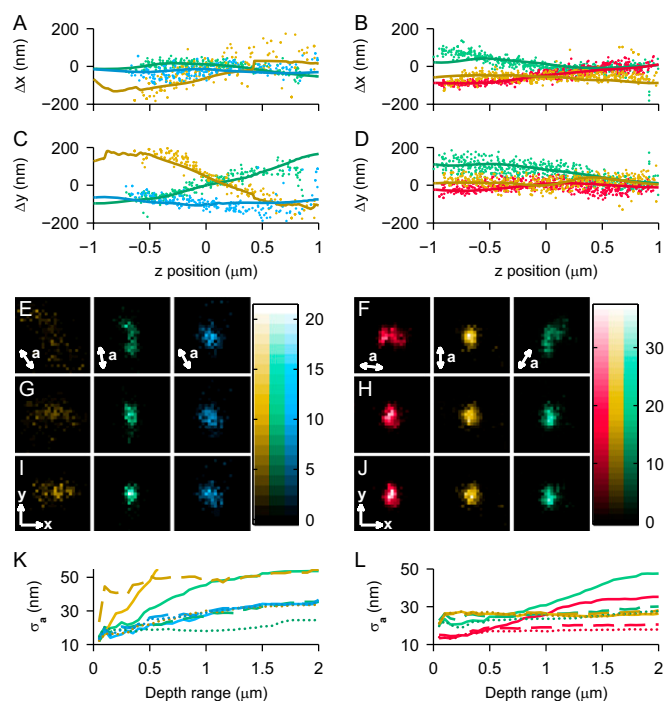


Fig. 4. Measured and predicted $(\Delta x, \Delta y)$ caused by dipole orientation effects for example molecule 1 (A, C, E, G, I, and K) and molecule 2 (B, D, F, H, J, and L). Color code is the same as in Fig. 3. (A–D) Measured (scatter points) Δx and Δy vs. z for each example molecule, with overlay (solid line) of simulated shift based on the mean extracted orientation. For each molecule, one mask orientation/polarization combination did not produce meaningful localizations because of low signal and/or high LA (omitted channels). (E and F) 2D histogram of uncorrected $(x_{\text{apparent}}, y_{\text{apparent}})$ localizations over the 2- μm DR. In each panel, a is the predominant direction of lateral shift for that mask orientation/polarization channel. Bin size, 15 nm. (G and H) Corresponding 2D histograms of the corrected localizations as produced by subtracting each predicted $(\Delta x, \Delta y)$ based on each individual estimation of (θ, ϕ) . (I and J) The corrected 2D histograms produced by subtracting the predicted $(\Delta x, \Delta y)$ based on the average estimation of (θ, ϕ) . Displayed (x, y) axes are 100 nm in length. (K and L) Additional quantification of the improvement in lateral localization showing σ_a , the SD along the direction a in each channel, as a function of DR about the focal plane. We compare σ_a calculated for the uncorrected case (solid line), the individual measurement-based correction (dashed line), and the average-based correction (dotted line).

fewer photons detected in this channel make for a more diffuse corrected histogram than in other cases.

Large values of LA can also affect the precision of position measurements, because the midpoint between one very bright and one very dim lobe is difficult to localize. Commonly in our experiment, a combination of few detected photons and large LA made spatial localizations in one of four mask orientation/polarization channels highly erratic (omitted cases in each example molecule). However, we still obtained meaningful estimates of LD and LA from such cases that were highly valuable in the extraction of (θ, ϕ) . These orientation estimates, in turn, resulted in shift corrections that improved the localizations in channels that did have meaningful (x, y, z) fits. There is, thus, a tradeoff between the benefit of being able to fit orientation and correct dipole-induced shifts and the cost of splitting photons into multiple channels.

For additional improvement in correction, Fig. 4 *I* and *J* shows the results of using the average values of all measurements of (θ, ϕ) to correct each localization. In general, this method improved the localizations slightly more than the individual measurement-based method, because it makes use of a less noisy correction vector. The individual measurement-based method is more practical, however, because it requires far fewer measurements and therefore, is easier to adapt for use in a SMACM measurement. Taken together, these observations suggest that an individual set of four images is sufficient to correct the bulk of the dipole-induced shift for a molecule but that this correction can be improved somewhat if it is possible to measure the same molecule several times at multiple z positions.

As a final quantification, we also calculated the SD of (x, y) localizations along the lateral direction \mathbf{a} for each channel and molecule over various ranges in z (Fig. 4 *K* and *L*). The axis \mathbf{a} for each case is depicted in the lower left of each panel in Fig. 3 *E* and *F*, and it was determined by treating the 2D distribution as an ellipse and finding its major axis. Thus, a large σ_a implies a systematic apparent shift along the direction \mathbf{a} . A corrected distribution should remove the systematic shift and therefore, should reduce σ_a to the SD expected from photon-limited precision. Data for a given DR about the focal plane were calculated by including all localizations for which $|z|$ was less than that DR/2. As expected, in each case for which the deviation along \mathbf{a} was relatively large, the corrected values were markedly improved, especially at large DR. Table S2 summarizes the σ_a values calculated at the full 2- μm DR and compares them with the σ expected from photon-limited precision. For example, in the green channel of molecule 1, the uncorrected σ_a (54 nm) was three times larger than the statistical localization precision (18 nm). The individual measurement-based correction improved σ_a to 35 nm, whereas the average-based method improved it further to 24 nm. In the gold channel of molecule 1, the large (>200 nm) shift produced an uncorrected σ_a of 116 nm (vs. 28-nm precision along that direction). Individual correction reduced this number by more than a factor of two (55 nm), whereas the average correction brought σ_a to within 6 nm of the precision (34 nm) along that direction. This channel is still relatively diffuse along the x direction on correction, however, because of limited photon detection (the DH-PSF in general gives unequal σ_x and σ_y , because it is not circularly symmetric) (27). In the green channel of molecule 2, σ_a (48 nm) was nearly two times as large as the precision (25 nm). This SD was corrected to within 5 nm of the precision in both the individual correction (30 nm) and the average correction (28 nm). Similarly, the red channel of molecule 2 gave uncorrected, individually corrected, and average corrected σ_a values of 35, 21, and 18 nm compared with a precision of 17 nm.

In some cases (e.g., the red channel of molecule 2), we found that the corrected value was actually slightly worse at small DR but still much better at sufficiently high DR. This effect suggests that an efficient algorithm that corrects orientation effects in a SMACM experiment will only apply corrections in cases in which it is beneficial (e.g., at large $|z|$, molecules with inclined orientations, and polarization channels with a high enough

signal-to-background ratio). Overall, these results show that the DH-PSF has the powerful ability to correct large lateral position errors caused by the SM dipole effect over an extended 2- μm DR.

Conclusion and Outlook

With this direct experimental demonstration, we show that the DH-PSF can be used to simultaneously extract precise 3D localization, estimate dipole orientation, and dramatically reduce (x, y) systematic errors caused by the orientation effect over an extended z range. Although our method requires two camera exposures for every set of measurements, our SLM can alternate phase mask orientations programmatically at speeds of at least 30 Hz (limited by the liquid crystal composition of our SLM). Different phase modulators can be toggled faster. Additionally, an optical setup containing separate phase masks for each polarization channel may be able to provide orientation from just a single acquisition using a slightly modified analysis.

This proof of principle shows that our method works best for correcting shifts of intermediately inclined molecules ($\sim\theta \in [35^\circ, 75^\circ]$). Our method has more difficulty fitting the orientations of less-inclined molecules ($\theta > 75^\circ$); because $|LA|$ is closer to zero for all z , there exist near-degeneracies in some of these cases (Fig. S4). However, this limitation is not likely to prohibit the correction of significant dipole-induced mislocalizations in SMACM experiments, because those same noninclined molecules produce negligible $(\Delta x, \Delta y)$ (Fig. S5). We did not encounter many very highly inclined molecules ($\theta < 35^\circ$) in our measurement, because both pumping and collection efficiencies are diminished for these cases (33). A standard SMACM experiment also would have difficulty detecting these molecules for the same reasons.

The theoretical limit of the DH-PSF's ability to extract position and orientation can be quantified using a Fisher information calculation; in particular, because the double-lobed shape of the DH-PSF is conserved over various dipole orientations and axial positions, the orientation precision of the DH-PSF is uniform over a large range of (z, θ, ϕ) (SI Text and Fig. S6). Thus, because the DH-PSF has been established as a highly precise method for 3D SMACM (28, 29), our orientation extraction/shift correction method to improve accuracy by removing systematic error is a good candidate to be incorporated into such experiments. As pointed out above, if labels are rotationally mobile, the dipole shift can be averaged out during an acquisition. At the other extreme, if labels are fixed in orientation during an acquisition, our method can be applied. The intermediate regime of rotational flexibility will be the subject of future work. Importantly, the fact that DH-PSF LA deviates from zero when SMs are fixed in their orientation and sufficiently inclined suggests that the DH-PSF can be used as a diagnostic tool in determining when labels are sufficiently rotationally mobile.

Although we found that we did not need to explicitly account for aberrations in the DH-PSF to yield good results for the examples given here, it may be necessary to address aberrations in the future to broaden the scope of our method and improve its performance. Finally, the DH-PSF-based orientation-sensing method may also be improved by using more sophisticated estimators and phase retrieval (34), particularly when high LA or aberrations make the DH-PSF deviate from its typical double Gaussian shape. With the correction of localization errors from the SM dipole orientation effect, far-field superresolution microscopy is one step closer to attaining molecular spatial resolution (~ 1 nm) (35) to reveal the nanoscale machinery at work within living cells.

Materials and Methods

Sample Preparation. Nanomolar concentrations of DCDHF-N-6 (31) were spun in a thin layer of 1% (by mass) PMMA of thickness 30–35 nm as measured by ellipsometry. Fluorescent beads (FluoSpheres, 100-nm diameter, 580/605; Invitrogen) were adhered directly to the air-polymer interface by spinning a dilute solution on top of the polymer layer and allowing it to dry. The beads served as both internal calibration markers for the DH-PSF response and fiducial markers for drift and sample tilt corrections (SI Text). They could

not be spun directly into the polymer matrix because of instability in organic solvents.

Imaging. Samples were mounted on an inverted Olympus IX71 fluorescence microscope, and the optical setup described in Fig. 1B was constructed outside the left-side port with the use of a phase-only spatial light modulator (Boulder Nonlinear Systems XY Phase Series). Fluorophores were excited with an Ar-ion laser emitting at 514 nm. The wide-field excitation beam was tilted at a slight angle to compensate for the dynamic range of brightness presented by the beads vs. the SMs. The laser was roughly circularly polarized (~1.4:1) at the sample. Molecules were irradiated at relatively low intensity (~0.1 kW/cm²) to ensure a full cycle of measurements before photobleaching. Fluorescence was collected through a 100× 1.4 N.A. oil-immersion objective (Olympus UPlan-SAPo 100×/1.40) and filtered using a Chroma Z514RDC dichroic and a 590/60 band pass. Images were recorded on an Andor iXon+ DU897-E EMCCD camera operating at an EM gain setting of 300.

For DH-PSF imaging, the sample was scanned over a z range of 2 μm at 50-nm spacing using an objective z positioner (C-Focus operating in open-loop mode; Mad City Labs). The DH-PSF mask was first loaded on the SLM with perpendicular orientation. Frames were recorded with 0.5-s exposures at 5 frames per z step. The loaded mask was then rotated 90° clockwise, and the sample was scanned again. After two full scans, the sample was refocused and then defocused by $1.00 \pm 0.15 \mu\text{m}$; therefore, the objective was moved away from the air-polymer interface. The coma/astigmatism correction mask (SI Text) for the transmitted channel was then loaded onto the SLM, and 10–30 1-s exposures were recorded. Then, the coma/astigmatism correction mask for the reflected channel was loaded, and another such series of images was recorded. This full process of scanning two times and then taking defocused snapshots was repeated until a field of view was sufficiently photobleached.

Analysis. Tiff image stacks were exported by the Andor Solis software and analyzed with custom MATLAB routines. Each analyzed molecule was picked by hand based on the presence of a single-step bleaching event (indicating an SM), sufficient local sparsity to avoid overlapping signals, and sufficient signal-to-noise ratio. A constant background offset was subtracted from each SM region, which was calculated from a user-defined local background region. The resulting image was fit to a double Gaussian (i.e., the sum of two

Gaussians) through nonlinear least squares regression using the MATLAB function `lsqnonlin` (SI Text). Simultaneously recorded gold and blue channel images (mask perpendicular) of an SM were paired with green and red channel images (mask parallel) of the same molecule based on z proximity. From each set of four images, the observables (x_{apparent} , y_{apparent} , z , LA , LD) were calculated. (x_{apparent} , y_{apparent}) were given by the midpoint position between the two lobes as determined by the double Gaussian fit along with a composite calibration correction to account for the nonideality of the DH-PSF response because of optical aberrations, sample tilt, stage drift, and the difference between the surrounding medium of the SMs vs. the medium of the fluorescent beads (SI Text and Fig. S7); z was given by the measured angle of the line connecting the centers of the two lobes relative to the horizontal, which was referenced to the calibrated response of the bead DH-PSF to the stepping of the stage by known amounts. LA was computed from the estimated amplitudes of the two Gaussians. LD was calculated from the total integrated photons above background in the region of the SM. If the automatic double Gaussian fit failed, the image was fit to two Gaussians by hand-selecting the regions of the two peaks. In this way, bounds or estimates of LA and LD could still be extracted and fed to the orientation look-up program even if (x , y , z) localizations were not reliable in that channel. To estimate (θ , ϕ) for each measurement of (z , LD , LA), the MATLAB function `lsqnonlin` was used to converge on the best (θ , ϕ) that minimized the difference between the measured LA and LD vs. predictions of the theoretical response of the DH-PSF (SI Text).

ACKNOWLEDGMENTS. We acknowledge Dr. Michael Thompson and Dr. Majid Badieirostami for assistance designing the experiments and writing simulation code. We also thank Dr. Sean Quirin for helpful discussions and Max Shulaker for ellipsometry measurements. M.P.B. acknowledges support from a Robert and Marvel Kirby Stanford Graduate Fellowship. M.D.L. acknowledges support from a National Science Foundation Graduate Research Fellowship and a 3Com Corporation Stanford Graduate Fellowship. A.S.B. acknowledges support from the National Defense Science and Engineering Graduate Fellowship. This work was supported by National Science Foundation Awards DBI-0852885 (to R.P.), DBI-1063407 (to R.P.), and DGE-0801680 (to R.P.), and by National Institute of General Medical Sciences Grant R01GM085437 (to W.E.M.).

- Moerner WE (2012) Microscopy beyond the diffraction limit using actively controlled single molecules. *J Microsc* 246(3):213–220.
- Hell SW (2009) Microscopy and its focal switch. *Nat Methods* 6(1):24–32.
- Betzig E, et al. (2006) Imaging intracellular fluorescent proteins at nanometer resolution. *Science* 313(5793):1642–1645.
- Hess ST, Girirajan TPK, Mason MD (2006) Ultra-high resolution imaging by fluorescence photoactivation localization microscopy. *Biophys J* 91(11):4258–4272.
- Rust MJ, Bates M, Zhuang X (2006) Sub-diffraction-limit imaging by stochastic optical reconstruction microscopy (STORM). *Nat Methods* 3(10):793–795.
- Sharonov A, Hochstrasser RM (2006) Wide-field subdiffraction imaging by accumulated binding of diffusing probes. *Proc Natl Acad Sci USA* 103(50):18911–18916.
- Ha T, Enderle T, Chemla S, Selvin R, Weiss S (1996) Single molecule dynamics studied by polarization modulation. *Phys Rev Lett* 77(19):3979–3982.
- Dickson RM, Norris DJ, Moerner WE (1998) Simultaneous imaging of individual molecules aligned both parallel and perpendicular to the optic axis. *Phys Rev Lett* 81(24):5322–5325.
- Enderlein J, Toprak E, Selvin PR (2006) Polarization effect on position accuracy of fluorophore localization. *Opt Express* 14(18):8111–8120.
- Engelhardt J, et al. (2011) Molecular orientation affects localization accuracy in super-resolution far-field fluorescence microscopy. *Nano Lett* 11(1):209–213.
- Gould TJ, et al. (2008) Nanoscale imaging of molecular positions and anisotropies. *Nat Methods* 5(12):1027–1030.
- Rosenberg SA, Quinlan ME, Forkey JN, Goldman YE (2005) Rotational motions of macro-molecules by single-molecule fluorescence microscopy. *Acc Chem Res* 38(7):583–593.
- Sosa H, Peterman EJG, Moerner WE, Goldstein LSB (2001) ADP-induced rocking of the kinesin motor domain revealed by single-molecule fluorescence polarization microscopy. *Nat Struct Biol* 8(6):540–544.
- Peterman EJG, Sosa H, Goldstein LSB, Moerner WE (2001) Polarized fluorescence microscopy of individual and many kinesin motors bound to axonemal microtubules. *Biophys J* 81(5):2851–2863.
- Huang B, Wang W, Bates M, Zhuang X (2008) Three-dimensional super-resolution imaging by stochastic optical reconstruction microscopy. *Science* 319(5864):810–813.
- Juette MF, et al. (2008) Three-dimensional sub-100 nm resolution fluorescence microscopy of thick samples. *Nat Methods* 5(6):527–529.
- Shtengel G, et al. (2009) Interferometric fluorescent super-resolution microscopy resolves 3D cellular ultrastructure. *Proc Natl Acad Sci USA* 106(9):3125–3130.
- Pavani SRP, et al. (2009) Three-dimensional, single-molecule fluorescence imaging beyond the diffraction limit by using a double-helix point spread function. *Proc Natl Acad Sci USA* 106(9):2995–2999.
- Ha T, Laurence TA, Chemla DS, Weiss S (1999) Polarization spectroscopy of single fluorescent molecules. *J Phys Chem B* 103(33):6839–6850.
- Peterman EJ, Sosa H, Moerner WE (2004) Single-molecule fluorescence spectroscopy and microscopy of biomolecular motors. *Annu Rev Phys Chem* 55:79–96.
- Patra D, Gregor I, Enderlein J (2004) Image analysis of defocused single-molecule images for three-dimensional molecule orientation studies. *J Phys Chem A* 108(33):6836–6841.
- Lieb MA, Zavislan JM, Novotny L (2004) Single-molecule orientations determined by direct emission pattern imaging. *J Opt Soc Am B* 21(6):1210–1215.
- Sick B, Hecht B, Novotny L (2000) Orientational imaging of single molecules by angular illumination. *Phys Rev Lett* 85(21):4482–4485.
- Toprak E, et al. (2006) Defocused orientation and position imaging (DOPI) of myosin V. *Proc Natl Acad Sci USA* 103(17):6495–6499.
- Mortensen KI, Churchman LS, Spudich JA, Flyvbjerg H (2010) Optimized localization analysis for single-molecule tracking and super-resolution microscopy. *Nat Methods* 7(5):377–381.
- Aguet F, Geissbühler S, Märki I, Lasser T, Unser M (2009) Super-resolution orientation estimation and localization of fluorescent dipoles using 3-D steerable filters. *Opt Express* 17(8):6829–6848.
- Thompson MA, Lew MD, Badieirostami M, Moerner WE (2010) Localizing and tracking single nanoscale emitters in three dimensions with high spatiotemporal resolution using a double-helix point spread function. *Nano Lett* 10(1):211–218.
- Lew MD, et al. (2011) Three-dimensional superresolution colocalization of intracellular protein superstructures and the cell surface in live *Caulobacter crescentum*. *Proc Natl Acad Sci USA* 108(46):E1102–E1110.
- Lee HL, Sahl SJ, Lew MD, Moerner WE (2012) The double-helix microscope super-resolves extended biological structures by localizing single blinking molecules in three dimensions with nanoscale precision. *Appl Phys Lett* 100(15):153701.
- Pavani SRP, DeLuca JG, Piestun R (2009) Polarization sensitive, three-dimensional, single-molecule imaging of cells with a double-helix system. *Opt Express* 17(22):19644–19655.
- Lord SJ, et al. (2007) Photophysical properties of acene DCDHF fluorophores: Long-wavelength single-molecule emitters designed for cellular imaging. *J Phys Chem A* 111(37):8934–8941.
- Ghosh S, Quirin SA, Grover G, Piestun R, Preza C (2012) Double helix PSF engineering for computational fluorescence microscopy imaging. *Proc SPIE* 8227:82270F.
- Sick B, Hecht B, Wild UP, Novotny L (2001) Probing confined fields with single molecules and vice versa. *J Microsc* 202(Pt 2):365–373.
- Quirin S, Pavani SRP, Piestun R (2012) Optimal 3D single-molecule localization for superresolution microscopy with aberrations and engineered point spread functions. *Proc Natl Acad Sci USA* 109(3):675–679.
- Pertsinidis A, Zhang Y, Chu S (2010) Subnanometre single-molecule localization, registration and distance measurements. *Nature* 466(7306):647–651.

Supporting Information

Backlund et al. 10.1073/pnas.1216687109

SI Text

Image Formation of an Electric Dipole Emitter. Our simulations model the simplified optical system depicted in Fig. S1, which is similar to systems depicted in refs. 1–3. Specifically, we consider an emitter embedded slightly below the surface of a polymer that is spin-coated on a glass coverslip. In this situation, the objective lens will collect forward propagating light emitted by the dipole in addition to backward propagating light that has been reflected by the air–polymer interface. Because the refractive index mismatch between the polymer and glass is minor ($n_{\text{glass}} = 1.518$ vs. $n_{\text{polymer}} = 1.49$), we ignore the effects of this interface. After the electric fields at the image plane have been calculated, it is straightforward to augment our simulations to account for polarization, aberrations, and the Double-Helix Point Spread Function (DH-PSF) mask.

Theoretical calculations that extend the pioneering work of Richards and Wolf (4) and predict the image formed by an emitter with a fixed dipole orientation embedded at or near an interface have been developed in the studies by Enderlein (5) and Böhmer and Enderlein (6). In addition, ref. 7 describes methods for simulating a freely rotating emitter or a cluster of tightly packed randomly oriented dipoles (such as a nanoscale fluorescent bead). Furthermore, refs. 8 and 9 describe the impact of subwavelength thin films on dipole emission. Subsequent investigations (10) showed the effects of layered media on the intensity distributions observed at the back focal plane and image plane of a high-N.A. optical system.

Our general strategy will be to decompose the emission pattern of the dipole into a basis of plane waves. The effects of the air–polymer interface and the image-forming optics will be determined for each plane–wave component, and the intensity distribution formed on a camera sensor will then be calculated by integrating over all of the plane–wave contributions that propagate through the imaging system. We begin by considering a dipole emitter embedded a distance z_0 below the surface of an air–polymer interface, with a fixed azimuthal orientation $\phi = \alpha$ and a polar angle of $\theta = \beta$. From ellipsometry measurements, we determined the polymer thickness z_0 to be 30–35 nm. If we consider the plane–wave component of this dipole’s emission with propagation direction given by $\hat{k} = \{\sin(\eta)\cos(\psi), \sin(\eta)\sin(\psi), \cos(\eta)\}$, where ψ and η are the azimuthal and polar orientations of the propagation direction, respectively, then the electric field associated with this wave is given by

$$\hat{E}(\eta, \psi) = \hat{e}_s [\sin(\beta)\sin(\psi - \alpha)E_s^\parallel(\eta)] + \hat{e}_p [\sin(\beta)\cos(\psi - \alpha)E_p^\parallel(\eta) + \cos(\beta)E_p^\perp(\eta)], \quad \text{[S1]}$$

where

$$\begin{aligned} E_s^\parallel(\eta) &= -n_{\text{glass}} [e^{-ikz_0 \cos(\eta)} + R_s(\eta)e^{ikz_0 \cos(\eta)}] \\ E_p^\parallel(\eta) &= n_{\text{glass}} \cos(\eta) [e^{-ikz_0 \cos(\eta)} - R_p(\eta)e^{ikz_0 \cos(\eta)}] \\ E_p^\perp(\eta) &= n_{\text{glass}} \sin(\eta) [e^{-ikz_0 \cos(\eta)} + R_p(\eta)e^{ikz_0 \cos(\eta)}] \end{aligned} \quad \text{[S2]}$$

In the above expressions, $\hat{e}_s = \{-\sin(\psi), \cos(\psi), 0\}$ and $\hat{e}_p = \{\cos(\psi)\cos(\eta), \sin(\psi)\cos(\eta), -\sin(\eta)\}$ are the unit vectors perpendicular to \hat{k} , with \hat{e}_s also perpendicular to the optical axis. The superscripts \parallel and \perp denote whether a given component of the E-field is parallel or perpendicular to the interface. The wave number is $k = 2\pi n_{\text{glass}}/\lambda$, and $R_s(\eta)$ and $R_p(\eta)$ are the

Fresnel reflection coefficients for s and p polarized waves at a polymer–air interface (these terms account for the portion of backward-propagating light reflected at the interface); $\lambda = 609$ nm for DCDHF-N-6 in poly(methyl methacrylate) (11). The effect of the optical imaging system is to map a plane wave with propagation direction \hat{k} to another plane wave with a new propagation direction $\hat{k}' = \{\sin(\eta')\cos(\psi'), \sin(\eta')\sin(\psi'), \cos(\eta')\}$. This mapping is determined by Abbe’s sine condition: $M \sin(\eta') = n_{\text{glass}} \sin(\eta)$; here, we assume an image formed in air with magnification M . The azimuthal coordinate is unchanged between input and output (i.e., $\psi' = \psi$). Finally, to determine the electric field present at the image plane, all angular contributions to the total field are integrated together. Closed-form expressions exist for the integration over ψ' ; however, the integration over η' must be done numerically. The following integral must be evaluated:

$$\begin{bmatrix} E_x(\rho, \phi) \\ E_y(\rho, \phi) \end{bmatrix} = \int_0^{\eta'_{\text{max}}} \sqrt{\frac{\cos(\eta')}{n_{\text{glass}} \cos(\eta)}} e^{-ikz_1 \cos(\eta')} \sin(\eta') \begin{bmatrix} e_x \\ e_y \end{bmatrix} d\eta'. \quad \text{[S3]}$$

Note that the image plane has been parameterized using polar coordinates (ρ, ϕ) and that the polarized components of the electric field are calculated for two orthogonal directions, x and y . In the above expression, the upper bound of integration is set by the maximally inclined plane wave that can be captured by the microscope objective, and it is determined by the objective’s numerical aperture ($NA = 1.4$) and magnification ($M = 100$): $\eta'_{\text{max}} = \sin^{-1}(NA/M) = .014$ rad. Furthermore, the amount of defocus is given by z_1 . [Focusing beyond the emitter (i.e., moving the objective to the coverslip) corresponds to z_1 of positive sign.] The terms e_x and e_y are given by

$$\begin{aligned} e_x &= \frac{\sin(\beta)}{2} \left\{ J_0 \cos(\alpha) [\cos(\eta')E_p^\parallel - E_s^\parallel] \right. \\ &\quad \left. - J_2 \cos(2\phi - \alpha) [\cos(\eta')E_p^\parallel + E_s^\parallel] \right\} \\ &\quad - iJ_1 \cos(\beta) \cos(\phi) \cos(\eta') E_p^\perp \\ e_y &= \frac{\sin(\beta)}{2} \left\{ J_0 \sin(\alpha) [\cos(\eta')E_p^\parallel - E_s^\parallel] \right. \\ &\quad \left. - J_2 \sin(2\phi - \alpha) [\cos(\eta')E_p^\parallel + E_s^\parallel] \right\} \\ &\quad - iJ_1 \cos(\beta) \sin(\phi) \cos(\eta') E_p^\perp, \end{aligned} \quad \text{[S4]}$$

where $J_{0,1,2}$ are Bessel functions of the first kind with the argument $k'\rho \sin(\eta')$, and $k' = \frac{2\pi}{\lambda}$. Similar expressions exist for the magnetic fields. However, we assume that, for all of the propagation media, $\mu_r = 1$. For nonpolarization sensitive detection, the intensity distribution at the image plane may be calculated as

$$I(\rho, \phi) = \frac{c\epsilon_0}{2} [E_x(\rho, \phi)E_x^*(\rho, \phi) + E_y(\rho, \phi)E_y^*(\rho, \phi)]. \quad \text{[S5]}$$

Practically, the integral in Eq. S3 was computed using a rectangular approximation by substituting Eq. S2 into Eq. S4 and then evaluating the integrand at a fixed location (ρ, ϕ) while varying η' from zero to η'_{max} . Summing the results together yields the electric fields at the single point in the image plane (ρ, ϕ) . In our

simulations, $E_x(\rho, \varphi)$ and $E_y(\rho, \varphi)$ were evaluated within a 256×256 grid, with samples spaced a distance of $1 \mu\text{m}$ apart. (After accounting for the magnification factor of 100, the effective spacing at the focal plane is 10 nm .) Also, for each location within the image plane, the integrand was evaluated for 100 different values of η' spaced evenly between zero and η'_{max} (i.e., $\delta\eta' = .01 \times \sin^{-1}(1.4/100) = .00014 \text{ rad}$). Performing this calculation for an entire 256×256 region takes approximately 2 min running 32-bit MATLAB on a standard office desktop computer (Dell Optiplex 960 with a 3 GHz Intel Core 2 Duo CPU).

Equipped with a theoretical model describing the image formed by a dipole emitter, we may begin to make modifications to account for the particulars of our optical design. Because a polarizing beam splitter was used to record two orthogonal polarizations of the electric field in separate regions of an image sensor, the two polarized intensity distributions $[I_x(\rho, \varphi)$ and $I_y(\rho, \varphi)]$ are calculated as

$$\begin{bmatrix} I_x(\rho, \varphi) \\ I_y(\rho, \varphi) \end{bmatrix} = \frac{c\epsilon_0}{2} \begin{bmatrix} E_x(\rho, \varphi)E_x^*(\rho, \varphi) \\ E_y(\rho, \varphi)E_y^*(\rho, \varphi) \end{bmatrix}. \quad [\text{S6}]$$

Furthermore, the geometry of our setup causes light reflected by the beam splitter to incur one additional reflection as it propagates through the imaging pathway. Therefore, simulated images for one polarization must be reflected about the $\varphi = 90^\circ$ axis before comparison with acquired data. (Here, the x and y polarized simulations can be related to the T and R channels, respectively, by taking into account the appropriate reflections and rotations introduced by the experimental setup. Fig. 1B depicts the specific geometrical transformations that each polarized image undergoes before it is projected onto the image sensor.)

Modeling Dipole Emission Effects on the DH-PSF. To simulate how a dipole emitter undergoes phase modulation to form the DH-PSF, we use the same framework described above and numerically integrate Eq. S3. The electric fields were sampled with a different pixel size and number of samples from above to match the discrete pixels of the DH-PSF phase mask and avoid ringing artifacts of the discrete Fourier transform ($1,024 \times 1,024$ pixels, $5.95\text{-}\mu\text{m}$ pixel size in the image plane, 59.5-nm pixel size in the focal plane). The resulting electric fields at the image plane are calculated as

$$\begin{aligned} E_x^{DH-PSF}(\rho, \varphi) &= FT\left\{FT\{E_x(\rho, \varphi)\}e^{i\psi^{DH-PSF}(\rho', \varphi')}\right\} \\ E_y^{DH-PSF}(\rho, \varphi) &= FT\left\{FT\{E_y(\rho, \varphi)\}e^{i\psi^{DH-PSF}(\rho', \varphi')}\right\}. \end{aligned} \quad [\text{S7}]$$

In the above equation, $FT\{\}$ denotes the Fourier transform operation, whereas two cascaded Fourier transforms model the image formation process of a $4f$ optical system (12). The function $\psi^{DH-PSF}(\rho', \varphi')$ models the phase delay imparted by the DH-PSF pattern programmed into the spatial light modulator (SLM). In this simulation, the mask is oriented such that its discontinuities are along the x axis; therefore, the x polarization has parallel-type behavior, whereas the y polarization has perpendicular-type behavior. It is convenient to normalize the radial coordinate, ρ' , such that the electric field is zero at distances greater than $\rho' = 1$ from the center of the pupil. (If one were to use nonnormalized coordinates, $\rho' = 1$ corresponds to the distance fNA/M from the center of the aperture, where f is the focal length of the optical system.) Simulated polarized images of the DH-PSF (Fig. S2A and B), expressed as $I_x^{DH-PSF} \propto |E_x^{DH-PSF}|^2$ and $I_y^{DH-PSF} \propto |E_y^{DH-PSF}|^2$, were then fit by our double Gaussian estimator to map out the response of DH-PSF as a function of dipole orientation (θ, ϕ). The double Gaussian estimator finds the best-fitting param-

eters ($A_{L1,L2}, x_{L1,L2}, y_{L1,L2}, \sigma_{L1,L2}$) that minimize the summed square error between the function

$$\begin{aligned} I^{DG}(\rho, \varphi) &= A_{L1} \exp\left[\frac{-(\rho \cos \varphi - x_{L1})^2 - (\rho \sin \varphi - y_{L1})^2}{2\sigma_{L1}^2}\right] \\ &+ A_{L2} \exp\left[\frac{-(\rho \cos \varphi - x_{L2})^2 - (\rho \sin \varphi - y_{L2})^2}{2\sigma_{L2}^2}\right] \end{aligned} \quad [\text{S8}]$$

and the simulated DH-PSF images I_x^{DH-PSF} and I_y^{DH-PSF} using the optimization function `lsqnonlin`. ($A_{L1,L2}, x_{L1,L2}, y_{L1,L2}, \sigma_{L1,L2}$) are the fitted amplitudes, x position, y position, and widths (SD), respectively, of each Gaussian lobe of the DH-PSF. The double Gaussian estimator produced reasonable fits of the DH-PSF for most dipole orientations (Fig. S2C and D). The spatio-orientation space (z, θ, ϕ) was sampled at a rate of ($\delta z = 50 \text{ nm}$, $\delta \theta \cong 6.5^\circ$, $\delta \phi \cong 6.5^\circ$), which is shown as black dots in Fig. S2E, column 1. Observable parameters of the DH-PSF for orientation fitting were then calculated from the double Gaussian fit parameters using the relations

$$LD(z, \theta, \phi) = \frac{N_x - N_y}{N_x + N_y}, \quad [\text{S9}]$$

$$LA(z, \theta, \phi) = \frac{A_{L1} - A_{L2}}{A_{L1} + A_{L2}}, \quad [\text{S10}]$$

$$\Delta x(z, \theta, \phi) = \frac{x_{L1} + x_{L2}}{2}, \quad [\text{S11}]$$

and

$$\Delta y(z, \theta, \phi) = \frac{y_{L1} + y_{L2}}{2}, \quad [\text{S12}]$$

where N_x and N_y are the total number of photons in the x and y polarization channels, respectively. Linear dichroism LD was found to have essentially no dependence on emitter defocus z (Fig. 2B), but lobe asymmetry LA (Fig. S2E and F) and lateral shifts ($\Delta x, \Delta y$) (Fig. S2G–J) have diverse behavior across (z, θ, ϕ). Notably, it is the contrasting behavior between LA in the x and y channels [termed the parallel (Fig. S2E) and perpendicular (Fig. S2F) behaviors in the text] that breaks the degeneracy of LD and enables effective measurement of orientation with the DH-PSF.

Modeling and Correction of Optical Aberrations. Our objective lens and relay optics induced a slight amount of spherical aberration in the images recorded on the electron-multiplying charge-coupled device (EMCCD) camera. Simulations of the standard PSF were augmented accordingly by applying a spherical aberration phase mask to the electric field that we calculated to be present at the pupil (aperture) plane of our microscope. We found the aberrated electric fields for x and y polarizations simply by taking the Fourier transform of the unaberrated fields present at the image plane, multiplying by the appropriate phase mask, and then inverse Fourier transforming:

$$\begin{aligned} E_x^{Sph.Ab.}(\rho, \varphi) &= IFT\left\{FT\{E_x(\rho, \varphi)\}e^{i\psi^{Sph.Ab.}(\rho', \varphi')}\right\} \\ E_y^{Sph.Ab.}(\rho, \varphi) &= IFT\left\{FT\{E_y(\rho, \varphi)\}e^{i\psi^{Sph.Ab.}(\rho', \varphi')}\right\}. \end{aligned} \quad [\text{S13}]$$

$IFT\{\}$ denotes the inverse Fourier transform operation. The aberration function $\psi^{Sph.Ab.}(\rho', \varphi')$ models the phase delay effects of

spherical aberration. Using the ρ' coordinate system, first-order spherical aberration is given explicitly by the polynomial (13)

$$\psi^{Sph.Ab.}(\rho', \phi') = A(6\rho'^4 - 6\rho'^2 + 1). \quad [\text{S14}]$$

The coefficient A sets the magnitude of aberration present in the system. We determined this coefficient heuristically. Interestingly, the incorporation of spherical aberration into the simulated images only improved matches with the clear-aperture defocused PSFs, and therefore, it was only included there. Accounting for spherical aberration did not improve matches to simulated DH-PSF images and therefore, was omitted for this part of the analysis.

The clear-aperture defocused PSFs also exhibited elements of astigmatism and comatic aberration. Instead of incorporating these effects in simulation, we corrected these distortions experimentally using the same SLM that was used to create the DH-PSF. Because coma and astigmatism are inherently asymmetric and lead to more dramatic distortions in the defocused PSF, we found it more expedient to experimentally diagnose and remove these aberrations. In-house software was developed for loading coma and astigmatism phase masks onto the SLM and adjusting the magnitude of their aberration coefficients. We used phase masks of the form

$$\begin{aligned} \psi^{Coma}(\rho', \phi') &= B(3\rho'^3 - 2\rho')\cos(\phi' - \phi^{Coma}) \\ \psi^{Astig.}(\rho', \phi') &= C\{6\rho'^2\cos[2(\phi' - \phi^{Astig.})]\}. \end{aligned} \quad [\text{S15}]$$

To find optimal values for the parameters B , C , ϕ^{Coma} , and $\phi^{Astig.}$, data from our EMCCD was displayed in real time, and the SLM driving software was used to modify the aberration coefficients to minimize irregularities in the PSF. Because of the unique geometry of our optical setup, the SLM appears to have different orientations when viewed in each polarization channel. Furthermore, the imaging pathways for the two different polarizations induced slightly different aberrations. Therefore, it was necessary to image the x and y polarized images of defocused molecules sequentially, with different phase masks loaded onto the SLM to correct the aberrations present in each of the separate imaging paths. When recording DH-PSF data, we observed that the 3D PSFs were more robust to the effects of minor aberrations, and no experimental corrections were required.

Single-Molecule Orientation and 3D Position Estimation with the DH-PSF. As discussed in *Materials and Methods*, $(x_{\text{apparent}}, y_{\text{apparent}}, z, LA, LD)$ was measured for each single molecule (SM) in each detection channel (red, gold, green, and blue in the text) by fitting SM DH-PSF images with a double Gaussian estimator. This estimator is identical to the one used for the simulated DH-PSF response and is detailed above. SM orientation and position measurements were completed in two steps. First, orientation was estimated using the measured z position, lobe asymmetry, and linear dichroism across the four detection channels. Next, given this orientation, the calculated $(\Delta x, \Delta y)$ shift from simulations was subtracted from $(x_{\text{apparent}}, y_{\text{apparent}})$ to yield the true lateral position of the SMs.

The orientation measurement process was carried out as follows. Calibrated measurements of (z, LA, LD) from each channel were grouped together such that their measured z positions were within 50 nm of each other. (Channels with a double Gaussian fit that failed because of severe lobe asymmetry had their lobe asymmetry measured by hand-designating each Gaussian spot of the DH-PSF and fitting it to a 2D Gaussian function). The measurements $(z_{\text{meas},i}, LA_{\text{meas},i}, LD_{\text{meas},i})$ from all channels i were input to the orientation-fitting algorithm, which used the MATLAB function `lsqnonlin` to find the orientation (θ, ϕ) that minimizes

$$\sum_{i=1}^4 \left\{ w(LA_{\text{sim}}(z_i, \theta, \phi)) [LA_{\text{meas},i} - LA_{\text{sim}}(z_i, \theta, \phi)]^2 + [LD_{\text{meas},i} - LD_{\text{sim}}(z_i, \theta, \phi)]^2 \right\}, \quad [\text{S16}]$$

the weighted squared difference between measurements and simulations of LA and LD , where the index i refers to measurements from each of the four channels,

$$w(x) = \begin{cases} 1, & |x| < \frac{2}{3} \\ 3(1 - |x|), & |x| \geq \frac{2}{3} \end{cases}, \quad [\text{S17}]$$

the subscripts *meas* and *sim* refer to experimental and theoretical values, respectively, and $z_i = z_{\text{meas},i} + z_{\text{offset},i}$ is a calibrated z position that compensates for relative defocus between polarization channels of the $4f$ system. The piecewise linear-weighting function $w(x)$ serves to deemphasize simulated values of LA that are difficult to measure because of low signal-to-noise ratio (i.e., LA is deemphasized when $|LA| > \frac{2}{3}$). Explicitly, $LD_{\text{meas},i}$ is calculated from pairs of channels such that

$$LD_{\text{red}} = LD_{\text{green}} = \frac{N_{\text{red}} - N_{\text{green}}}{N_{\text{red}} + N_{\text{green}}} \quad [\text{S18}]$$

and

$$LD_{\text{gold}} = LD_{\text{blue}} = \frac{N_{\text{gold}} - N_{\text{blue}}}{N_{\text{gold}} + N_{\text{blue}}}. \quad [\text{S19}]$$

Finally, $z_{\text{offset},i}$ is calibrated for each measured SM by finding the best value that allows measurements of LA to overlap with calculated values of LA for the entire z scan. Because of local sample tilt, this value is slightly different for each SM that we measured. For molecule 1, $z_{\text{offset}} = 70$ nm for the transmitted polarization channels, and $z_{\text{offset}} = 200$ nm for the reflected polarization channels. For molecule 2, $z_{\text{offset}} = 0$ nm for the transmitted polarization channels, and $z_{\text{offset}} = -200$ nm for the reflected polarization channels. For molecule 3, $z_{\text{offset},T} = 186$ nm, and $z_{\text{offset},R} = -185$ nm. For molecules 4, 5, and 6, $z_{\text{offset},T} = z_{\text{offset},R} = 0$ nm. For positions and orientations (z_i, θ, ϕ) where simulations were not explicitly carried out, the MATLAB interpolation function `TriScatteredInterp` was used to evaluate $LA_{\text{sim}}(z_i, \theta, \phi)$ and $LD_{\text{sim}}(z_i, \theta, \phi)$. The above orientation estimator is a first-order approach that matches experimental data to a library of simulated data to measure orientation; more sophisticated optimization functions or finer sampling of simulated data may improve orientation-fitting performance.

When matching experimental measurements of (z, LA, LD) to simulations, care must be taken in ensuring that ϕ is transformed appropriately considering the optical system and orientation of the DH-PSF mask. Mapping ϕ_{IIP} in the intermediate image plane (IIP) (Fig. 1B) to a specific orientation relative to the DH-PSF mask (ϕ_{mask}), we obtain the following relations:

$$\begin{aligned} \phi_{\text{red,mask}} &= \phi_{\text{IIP}} \\ \phi_{\text{gold,mask}} &= \phi_{\text{IIP}} + \pi/2 \\ \phi_{\text{green,mask}} &= 3\pi/2 - \phi_{\text{IIP}} \\ \phi_{\text{blue,mask}} &= -\phi_{\text{IIP}} \end{aligned} \quad [\text{S20}]$$

Furthermore, the red and green channels show parallel-type behavior (Fig. 1B *Inset*) because their polarization is parallel to the

phase discontinuities of the DH-PSF mask, whereas the gold and blue channels show perpendicular-type behavior.

Two strategies for calculating the true lateral position of each SM were used. The first strategy uses measurements of $(z_{meas,i}, LA_{meas,i}, LD_{meas,i})$ at a single z position from all four channels i to measure orientation (θ, ϕ) . Then, the calculated $[\Delta x_i(z_i, \theta, \phi), \Delta y_i(z_i, \theta, \phi)]$ shift from simulations is subtracted from the apparent position $(x_{apparent,i}, y_{apparent,i})$ for each channel to recover the true location of the molecule. The second strategy involves averaging all such pointwise measurements of orientation over the entire z scan to yield $(\bar{\theta}, \bar{\phi})$. Then, the calculated shift $[\Delta x_i(z_i, \bar{\theta}, \bar{\phi}), \Delta y_i(z_i, \bar{\theta}, \bar{\phi})]$ for this single orientation $(\bar{\theta}, \bar{\phi})$ is used to correct the lateral position of the SM. This approach has the benefit of reducing orientation measurement noise at the cost of requiring multiple snapshots of each SM. Again, the MATLAB interpolation function `TriScatteredInterp` was used to evaluate $[\Delta x_i(z_i, \theta, \phi), \Delta y_i(z_i, \theta, \phi)]$.

Clear-Aperture Defocused Image Template Matching. By matching simulations to the image of a defocused molecule (without the DH-PSF), a well-established SM orientation determination method, we gain an independent estimate of that molecule's dipole orientation. This information is used for verification of our DH-PSF-based orientation estimation algorithms. Data were compared with a list of simulated templates. The dipole orientation of a defocused molecule was then estimated as the orientation of the template that yielded the closest fit to the actual data.

Using the simulation methods described above, a list of templates was generated for both the x and y polarized images of a defocused molecule. This template list included dipole emitters simulated at all orientations of θ from 0° to 90° and ϕ from 0° to 355° spaced at intervals of 5° . Hence, 1,368 pairs of polarized intensity distributions were simulated. In practice, all dipole emission patterns were calculated using MATLAB. Spherical aberration was simulated by first calculating the unaberrated high-resolution electric fields of an emitter with fixed orientation at the image plane. The result was zero-padded to ensure adequate sampling in the Fourier domain, and then, it was discrete Fourier-transformed using MATLAB's `fft2` function. The appropriate phase masks were applied as described above, and then, an inverse Fourier transform was applied using MATLAB's `ifft2` function to recover the aberrated image. By visually comparing simulations with acquired data, we found that the spherical aberration coefficient $A = 1.8$ yielded simulated images that closely matched experiment (Eq. S14). Furthermore, by comparing simulation with experiment, we estimated the defocus to be $1 \pm 0.15 \mu\text{m}$ below the emitter. (For a given field of view, the precise defocus depth was estimated by eye to generate a set of templates). To account for the pixelation effects of the EMCCD, simulations were performed on a high-resolution discretization of the image plane (256×256 - μm extent with 1×1 - μm sampling, which is equivalent to $2.56 \times 2.56 \mu\text{m}$ with 10×10 -nm pixels in object space). Subdivisions were made in the high-resolution grid ($16 \times 16 \mu\text{m}$ corresponding to 160×160 nm in object space), and intensity values within each subdivision were summed together. This summation leads to 16×16 -pixel templates that match the actual pixel size of our EMCCD. Each pair of polarized images was then normalized by the sum of the squares of its pixel values [that is, if I_x^j and I_y^j denote the x and y polarized images corresponding with the j th template in our list, the normalized templates are calculated as

$$\tilde{I}_x^j = \frac{I_x^j}{\sqrt{\sum_{m=1}^M \sum_{n=1}^M (I_x^j[m,n])^2 + (I_y^j[m,n])^2}}, \quad \text{[S21]}$$

$$\tilde{I}_y^j = \frac{I_y^j}{\sqrt{\sum_{m=1}^M \sum_{n=1}^M (I_x^j[m,n])^2 + (I_y^j[m,n])^2}}.$$

The additional brackets are used to denote the $[m,n]$ th pixel in an image, and M is the total number of pixels along a given dimension in the template (in this case, $M = 16$).

The normalized template that most closely matched the defocused images was determined as follows. A 16×16 region of interest was drawn around the image made by both the x and y polarized intensities (T and R channels, respectively, of Fig. 1B) of an SM. Background intensity was estimated by calculating the mean number of photons per pixel detected in a manually selected rectangle of $\sim 20 \times 20$ to 40×40 pixels nearby the molecule of interest and subsequently subtracted from each pixel in the region of interest containing the single defocused molecule. The cross-correlation between each of the two background-subtracted polarized images, D_x and D_y , and each template of generated images was then computed. The maximum values of the two resulting cross-correlation matrices were summed together, and the result, C_j , was stored. Mathematically, we evaluated

$$C_j = \max_{p,q} \left(\sum_{m=1}^M \sum_{n=1}^M D_x[m,n] \tilde{I}_x^j[m+p,n+q] \right) + \max_{p,q} \left(\sum_{m=1}^M \sum_{n=1}^M D_y[m,n] \tilde{I}_y^j[m+p,n+q] \right). \quad \text{[S22]}$$

This operation can be performed efficiently using MATLAB's `xcorr2` function. After C_j was computed for the entire template list, the template yielding the largest value of C_j was chosen as the best match, and the dipole orientation of that template was used as an estimate of the dipole orientation of the data. Fig. S3 shows the results of using template matching to estimate dipole orientation for the two molecules examined in the text. Representative image acquisitions are plotted with the simulated images of the templates that yield the best match. For both molecules, a defocus of $z_f = 1.13 \mu\text{m}$ was used to generate a list of templates. To benchmark the precision of this technique, orientation was estimated repeatedly for the same molecule using data from successive acquisitions. The mean orientation estimates and SDs in θ and ϕ were calculated (*Results and Discussion*).

Cramer–Rao Lower Bound for the Polarization-Sensitive DH System.

In the text, we presented the polarization-sensitive DH microscope as a means to simultaneously measure 3D position and orientation of an SM. Here, we quantitatively compare this approach with established methods that use a clear-aperture standard PSF system (1, 7). We calculate the photon-limited precision that can be achieved in estimating the position and orientation of a dipole using the Cramer–Rao Lower Bound (CRLB) (14).

The CRLB is defined as the inverse of the Fisher Information (FI) matrix, which assesses the information contained in a probability distribution for estimation of parameters. The FI matrix is additive; therefore, for a multiple channel system, the FI matrix of each channel is summed to get the total FI and then inverted to get the CRLB. The lower bound SD (σ_{LB}), which is the square root of the CRLB, directly yields a lower bound for the precision of an unbiased estimator in the same units as the measured data.

Thus, for the five-parameter estimation problem, the σ matrix is a 5×5 matrix. For 3D imaging and localization, we are interested in the minimum localization volume. One measure of this uncertainty volume is

$$\sigma_{3D} = \frac{4\pi}{3} \sigma_x \cdot \sigma_y \cdot \sigma_z. \quad [\text{S23}]$$

For the CRLB simulation, the dipole is assumed to be immersed in a medium of index 1.52 (no interface) and emitting at $\lambda = 610$ nm. The objective lens has an N.A. of 1.4. The pixel size is 160 nm in the object plane. We assume the imaging system to be shift-invariant, which is a good approximation in the central region of the field of view. The number of photons collected by the objective lens depends on the dipole's polar orientation. CRLB calculations show that most photons are collected when the dipole is oriented along $\theta = 90^\circ$, and thus, for photon-limited systems, all images are normalized according to this case (same number of photons emitted). The total number of photons detected for the dipole along $\theta = 90^\circ$ is taken to be 5,000, and all calculations are performed in the shot noise limit. In all calculations, the number of photons detected in the standard system is the same as the number in the DH system properly divided among the four channels.

Fig. S6A shows the localization and orientation error lower bound as a function of θ with and without background. The amount of defocus for either system is chosen to optimize the precision based on the lowest CRLB. Thus, the axial defocus for the standard (clear aperture) system is $z = 100$ nm, whereas the DH system performs best at focus ($z = 0$). Our calculations also show that σ_{3D} , σ_θ , and σ_ϕ are relatively constant as a function of the polar angle θ . To make a fair comparison, we choose $\phi = 45^\circ$ in Fig. S6A to evenly distribute the light between the two linear polarization channels.

The lower bound of the error for angle estimation and 3D position using the four-channel polarization-sensitive DH system is substantially lower than the lower bound of the standard PSF case. As expected, with the inclusion of background, the localization precision of the DH worsens, but it still performs better than the standard case for intermediate θ . The standard system performance is calculated for the optimal defocus, and therefore, it will substantially deteriorate with variations in z . On the contrary, the DH system has a slower variation with defocus and hence, provides a relatively uniform performance with defocus. The lower bound for estimating the angle and position as a function of defocus is shown in Fig. S6B and C. The dipole is oriented along a representative direction $(\theta, \phi) = (45^\circ, 45^\circ)$ in Fig. S6B and $(\theta, \phi) = (90^\circ, 90^\circ)$ in Fig. S6C. It can be seen that the DH system performs better than the standard system over most of the defocus range with and without background.

Calibrations. The behavior of the DH-PSF vs. z was calibrated using a fiducial fluorescent bead. Each field of view was chosen such that it included at least one fiducial bead near the edge of

the field. Laser power was kept sufficiently low such that the bead did not bleach appreciably during the experiment, which would otherwise make its emission increasingly anisotropic. LD of the beads was found to be $\sim 0.1 \pm 0.1$, justifying its use as an isotropic emitter. The microscope objective was then scanned in z as described in *Materials and Methods*. The angle made by the two lobes of the DH-PSF image of the bead at each z step was recorded to produce an angle vs. z calibration curve to be applied to the fit SMs (Fig. S7A), where $z = 0$ was assigned to 0° . Although the simulated DH-PSF of an isotropic point emitter does not translate in (x, y) as a function of z , factors such as sample tilt, aberrations, and imperfect mask alignment produce a baseline shift that must also be calibrated out of SM localizations to recover the true dipole-induced shifts (Fig. S7B and C). Because some of the factors that contribute to these calibration curves are different in each of the four mask orientation/polarization channel combinations, we used unique calibration curves for each channel (red, gold, green, and blue in the text).

Sample drift is another experimental effect that could potentially swamp the dipole-induced shifts that we sought to measure. By measuring a separate bead-based calibration curve for each individual z scan of each field of view, we mitigated this potential source of error. In this way, any (x, y) drift occurring during a scan was included in the (x, y) vs. z calibration. We measured multiple reproducible (x, y) shifts across all of our SM z scans, suggesting that drift was effectively removed.

The nanoscale behavior of the DH-PSF is subtly affected by the medium surrounding the SMs and fluorescent beads. As explained in *Materials and Methods*, sample constraints precluded the ability to embed the beads in the same medium as the SMs. Consequently, we measured nonzero residual (x, y) shifts for SMs with θ near 90° (we expect these shifts to be constant), even after applying the bead-based calibrations explained above. To calibrate and remove this residual shift, we chose two molecules with predicted shifts that were fairly constant measured experimentally to have polar orientations θ of $\sim 80^\circ$ and $\sim 85^\circ$. Calibration molecule 1 gave good signal in the reflected polarization channel, and therefore, we used the deviation between its measured (x, y) shifts and its predicted shifts to correct all SM shifts in the perpendicular/reflected (blue) and parallel/reflected (green) channels. Calibration molecule 2 gave good signal in the transmitted polarization channel, and therefore, it was used equivalently for the perpendicular/transmitted (gold) and parallel/transmitted (red) channels. We then applied third–eighth-order polynomial fits (chosen by using the lowest order that reproduced the major features as judged by eye) to these residual curves, effectively smoothing them. In cases where the curves needed to be extrapolated to span a full $2\text{-}\mu\text{m}$ depth of field, the smoothed curves were extended with a linear or low-order polynomial that gave the most qualitatively reasonable extrapolation. The measured residual shifts and their piecewise polynomial fits are displayed in Fig. S7D and E. These curves were subtracted from the measured shifts of all molecules in the appropriate channels.

- Patra D, Gregor I, Enderlein J (2004) Image analysis of defocused single-molecule images for three-dimensional molecule orientation studies. *J Phys Chem A* 108(33):6836–6841.
- Toprak E, et al. (2006) Defocused orientation and position imaging (DOPI) of myosin V. *Proc Natl Acad Sci USA* 103(17):6495–6499.
- Enderlein J, Toprak E, Selvin PR (2006) Polarization effect on position accuracy of fluorophore localization. *Opt Express* 14(18):8111–8120.
- Richards B, Wolf E (1959) Electromagnetic diffraction in optical systems. II. structure of the image field in an aplanatic system. *Proc R Soc Lond A Math Phys Sci* 253(1274):358–379.
- Enderlein J (2000) Theoretical study of detection of a dipole emitter through an objective with high numerical aperture. *Opt Lett* 25(9):634–636.
- Böhmer M, Enderlein J (2003) Orientation imaging of single molecules by wide-field epifluorescence microscopy. *J Opt Soc Am B* 20(3):554–559.
- Mortensen KI, Churchman LS, Spudich JA, Flyvbjerg H (2010) Optimized localization analysis for single-molecule tracking and super-resolution microscopy. *Nat Methods* 7(5):377–381.
- Lukosz W (1981) Light emission by multipole sources in thin layers. I. radiation patterns of electric and magnetic dipoles. *J Opt Soc Am* 71(6):744–754.
- Hellen EH, Axelrod D (1987) Fluorescence emission at dielectric and metal-film interfaces. *J Opt Soc Am B* 4(3):337–350.
- Axelrod D (2012) Fluorescence excitation and imaging of single molecules near dielectric-coated and bare surfaces: A theoretical study. *J Microsc* 247(2):147–160.
- Lord SJ, et al. (2007) Photophysical properties of acene DCDHF fluorophores: Long-wavelength single-molecule emitters designed for cellular imaging. *J Phys Chem A* 111(37):8934–8941.
- Goodman JW (2005) *Introduction to Fourier Optics* (Roberts & Company, Greenwood Village, CO).
- Mahajan VN (2007) *Optical Shop Testing*, ed Malacara D (Wiley, New York), pp 498–546.
- Kay SM (1993) *Fundamentals of Statistical Signal Processing: Estimation Theory* (Prentice Hall, Englewood Cliffs, NJ).

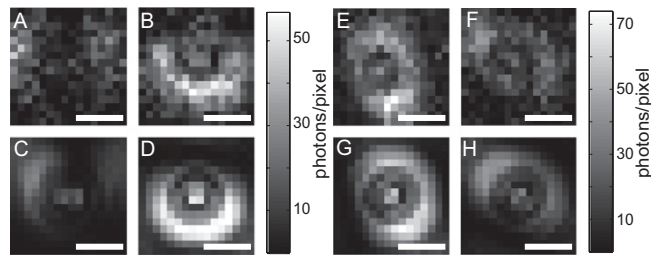


Fig. S3. Determining orientation from defocused images. *A* and *B* show representative acquisitions of molecule 1 in the *T* and *R* channels, respectively. *C* and *D* show the most closely matching set of polarized templates. *E* and *F* show *T* and *R* channel images of molecule 2, whereas *G* and *H* depict the best templates. For molecule 1, the mean orientation fit and SD were based on 72 separate 1-s acquisitions. For molecule 2, 27 acquisitions were collected before photobleaching. (Scale bars: 1 μm .)

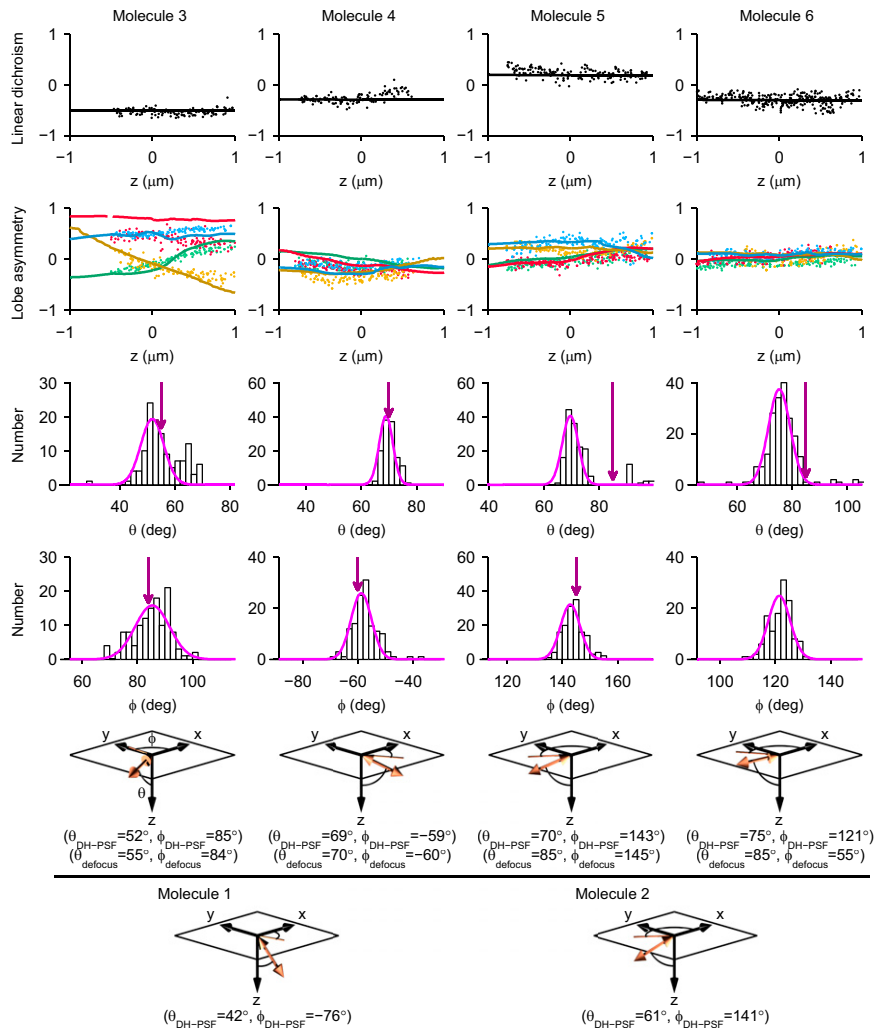


Fig. S4. Orientation estimations of additional molecules. In the top two rows, each measurement of *LD* and *LA* (scatter points) along with the predicted *LD* and *LA* (solid curve) based on the mean fit orientation of each molecule is shown. In the middle two rows, histograms of DH-PSF-based orientation estimations are overlaid with a Gaussian fit (magenta curve). Defocused clear-aperture estimates of orientation are denoted by purple arrows. In the bottom two rows, molecular orientation diagrams depict the measured orientations of molecules 3–6 as well as the orientations of molecules 1 and 2 from the text for comparison. Both molecules 3 and 4 have intermediate inclination, $\theta \in (35^\circ, 75^\circ)$, and therefore, they are well fit by the DH-PSF method. Molecules 3 and 4 show excellent agreement between the orientations estimated by the DH-PSF and the orientations estimated from defocused image template matching. Molecules 5 and 6 are not inclined much at all ($\theta > 75^\circ$), and therefore, the DH-PSF method does not yield orientation estimates that agree as well. Small values of $|LA|$ lead to degeneracies in the estimated parameters for these molecules. However, for the purpose of correcting dipole-induced mislocalizations, this fact is not of much importance, because noninclined molecules have negligible shifts (Fig. S5).

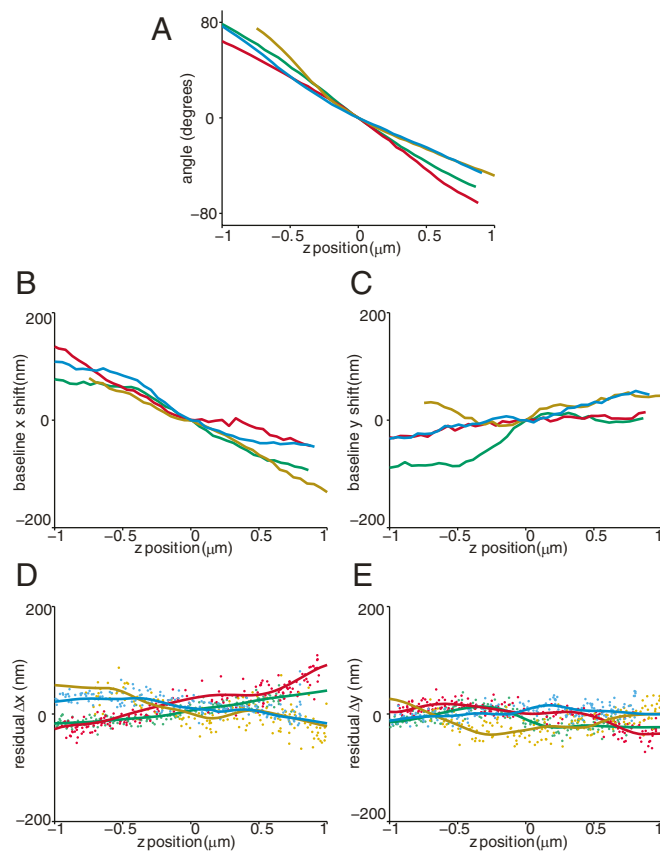


Fig. S7. Calibration curves used in SM fitting. Color code is same as in Figs. 3 and 4. (A) Angle made by two DH-PSF lobes vs. z as measured from a fluorescent bead. Different optical paths and different lateral offsets of the phase mask make for different curves in the four channels. (B and C) Baseline x and y vs. z curves. Nonidealities such as sample tilt, aberrations, and lateral mask offset cause a nonzero lateral shift in the PSF, even for an isotropic emitter, which must be subtracted out. (D and E) Residual lateral shifts vs. z . Because the fiducial beads are embedded in a slightly different medium, application of just the bead calibration curves leaves some residual shift for SMs that is caused by factors other than dipole orientation. Residual lateral shift calibration curves are calculated by subtracting the predicted shifts from the apparent shifts of two calibration molecules (*SI Text*).

Table S1. Average photons detected above background in each channel for each molecule

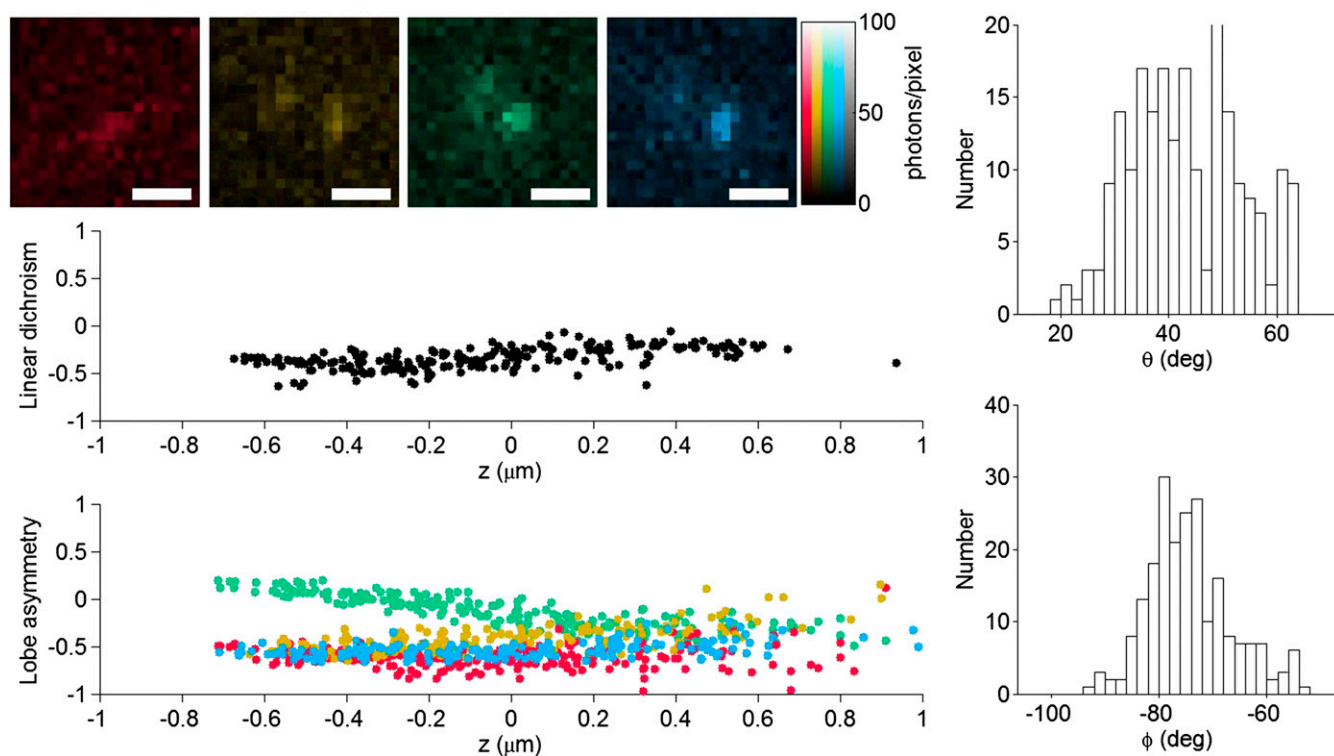
Molecule no.	Green	Red	Gold	Blue	Total
1	1,100	700	510	1,300	3,610
2	1,900	2,600	2,100	2,200	8,800
3	2,200	240	820	2,600	5,860
4	2,000	1,400	1,200	1,900	6,500
5	1,300	2,100	1,800	1,300	6,500
6	1,600	930	650	1,100	4,280
Mean total					5,925

Calculated by integrating all photons within a 15×15 -pixel box containing the molecule and subtracting the average background photons contained in this area. Average background for each molecule was determined by measuring the background in a nearby hand-designated region (~ 9 photons/pixel per frame average across all molecules).

Table S2. σ_a at 2- μm depth range for molecules 1 and 2 compared to localization precision

	Green		Red		Gold		Blue	
	σ_a (nm)	σ_a /precision						
Molecule 1								
Uncorrected	54	3	—	—	116	4.1	36	1.4
Individually corrected	35	1.9	—	—	55	2	37	1.5
Mean corrected	24	1.3	—	—	34	1.2	36	1.4
Precision	18	—	—	—	28	—	25	—
Molecule 2								
Uncorrected	48	1.9	35	2.1	26	0.96	—	—
Individually corrected	30	1.2	21	1.2	28	1	—	—
Mean corrected	28	1.1	18	1.1	27	1	—	—
Precision	25	—	17	—	27	—	—	—

Precision was calculated by binning localizations into 100-nm z bins and taking the SD along a in each bin. These values were then averaged across all bins within the center $\sim 1 \mu\text{m}$ of the z range. Our corrections show significant improvement in cases that have $\sigma_a \sim 2\times$ larger than precision or worse (molecule 1, green and gold channels; molecule 2, green and red channels).



Movie S1. DH-PSF-based molecular orientation measurements of molecule 1 over two axial (z) scans. The raw DH microscope images from each of the four measurement channels (red, gold, green, and blue) are shown in the upper left. Linear dichroism (middle left) and lobe asymmetry (bottom left) are depicted as scatter points because they are measured during the scans. Finally, histograms of the calculated polar and azimuthal orientation of molecule 1 are plotted at right. The final frames of the movie show LD and LA (as solid lines) for the mean orientation measured for molecule 1 (center of the Gaussian fits at right).

[Movie S1](#)